RESEARCH ARTICLE

VOLCANICA

Eruptive flux drives atmospheric lightning rates and submarine hydroacoustic signals during the 2021 Fukutoku-Oka-no-Ba eruption

Kathleen F. McKee *[α,β], Kristen E. Fauria[α], Jackie Caplan-Auerbach[γ], Jelle D. Assink[δ], Mikkel Louis[α,ε], Tushar Mittal[ζ], Fukashi Maeno[η], Mie Ichihara[η], Dirk Metz[θ], and Chris Vagasky[ι]

[α] Department of Earth and Environmental Science, Vanderbilt University, Nashville, US.
[β] Now at Department of Geological and Mining Engineering and Sciences, Michigan Technological University, Houghton, Michigan, US.
[γ] Geology Department, Western Washington University, Bellingham, US.
[δ] R&D Department of Seismology and Acoustics, Royal Netherlands Meteorological Institute (KNMI), De Bilt, The Netherlands.
[ε] College of Earth, Ocean, and Atmospheric Sciences, Oregon State University, Corvallis, US.
[ζ] Department of Geosciences, Pennsylvania State University, State College, Pennsylvania, US.
[η] Earthquake Research Institute, the University of Tokyo, Tokyo, Japan.
[θ] Preparatory Commission for the Comprehensive Nuclear-Test-Ban Treaty Organization (CTBTO), Vienna, Austria.
[ι] College of Agricultural and Life Sciences, University of Wisconsin-Madison, Madison, US.

Submitted: 2025-04-28 | In Review | Accepted: 2026-04-27 | Published: 2026-02-11

Editor: O. Lamb | Typesetter: J. Farquharson

Abstract

The August 2021 eruption of Fukutoku-Oka-no-Ba (FOB) volcano in Japan was a remarkable VEI 4 shallow submarine eruption, partly because it generated a 16-km water-rich atmospheric plume, new islands, and a large pumice raft. Recent studies provide complementary summaries of the atmospheric and oceanic surface expressions of the 2021 FOB eruption, including analyses of regional infrasound and Himawari-8 geostationary satellite data. The hydroacoustic record has also been published. Following these studies, we examine how the processes occurring beneath the sea surface correlate with the intensity of the atmospheric portion of the 2021 FOB eruption. We compare multiple data sets, specifically International Monitoring System (IMS) hydroacoustic and infrasonic array data in the context of ground-based lightning observations, and plume height and width data (Himawari-8). We estimate a time-varying volumetric flow rate from plume observations and compare the resulting time series with acoustic and lightning characteristics. The infrasound data do not correlate with the other data streams due to signal loss from diurnal winds. The lightning, hydroacoustic, and volume-flux data are highly correlated, and we suggest this is because all three depend on eruption flux and intensity at the vent.

Keywords: Fukutoku-Oka-no-Ba; Hydroacoustic; Lightning; Volume Flux; Infrasound.

1 Introduction

Shallow (<~300 m) submarine explosive eruptions can breach the ocean surface and create large atmospheric plumes that, in turn, may impact air traffic and atmospheric aerosol loads. Recent examples include the 2022 eruption of Hunga Volcano, Tonga, which made the tallest atmospheric plume ever recorded at ~55 km [Carr et al. 2022; Gupta et al. 2022; Proud et al. 2022], increased the stratospheric water load by 10% [Vömel et al. 2022], and had detectable sulfate aerosols for 8 days after the eruption [Kahn et al. 2024; Gupta et al. 2025]. For these eruptions that reside in both the ocean and atmosphere, fundamental questions exist about the relationship between processes in the atmospheric plume and the marine environment, and the transition between the submarine and the aerial plume [Rowell et al. 2022; Mastin et al. 2024]. Here we examine the ~3-day long 2021 shallow submarine eruption of Fukutoku-Oka-no-Ba (FOB), Japan, which created a 16 km atmospheric plume, a ~0.1 km^3 pumice raft, and new islands [Maeno et al. 2022; Fauria et al. 2023] from a vent that was ~40 meters below sea level.

Although atmospheric plumes from eruptions like FOB can now be readily analyzed using satellite remote sensing with limitations such as cloud cover and sample rate (1 image per 10 minutes for most geostationary satellites), the eruptive processes under the ocean surface are difficult to quantify because we lack sensors on or near the seafloor at most submarine volcanoes [e.g., Tepp and Dziak 2021]. However, seismoacoustic signals that couple into the water column can travel great (>1000 km) distances in the sound-fixing and ranging (SOFAR) channel and can be measured using hydroacoustic arrays [Ewing and Worzel 1948; Bryan et al. 1963; Metz et al. 2016]. A central challenge lies in interpreting these hydroacoustic signals and understanding what processes, such as near-vent explosions or eruption-driven landslides or seismotectonic earthquakes, are recorded [e.g., Chadwick Jr. et al. 2008; 2012; Dziak et al. 2012; Caplan-Auerbach et al. 2017; Tepp and Dziak 2021, among others].

The 2021 eruption of FOB is a case in which the atmospheric component of the eruption can be well characterized in space and time using multiple datasets, including satellite imagery, infrasound, and lightning [e.g., Maeno et al. 2022; Fauria et al. 2023, among others]. Hydroacoustic arrays (H11N and H11S) at Wake Island, 2688 km from FOB, also recorded the hydroacoustic signals from the eruption [Metz 2022; Tanaka et al. 2025]. By comparing the timing and intensity of the atmospheric and submarine datasets, we seek to better understand the extent to which the submarine and atmospheric eruption processes were coupled. We hypothesize

* kfmckee@mtu.edu

that the eruptive flux at the shallow submarine vent controls the intensity of the atmospheric plume (as indicated by plume width, lightning rate, and infrasonic intensity) and the intensity of the hydroacoustic signals (as indicated by detection rate and amplitude). We apply a fluid-mechanics-based technique from Pouget et al. [2013] to assess temporal variations in the FOB eruption rate based on atmospheric plume width. By comparing these submarine and atmospheric data, we test the idea that near-vent processes control the intensity and duration of both submarine and atmospheric signals at FOB. The alternative is that the hydroacoustic data contains signals without parallels in the atmosphere, thus indicating the presence of purely submarine processes such as eruption-triggered underwater mass wasting or underwater jetting without a large aerial plume.

We aim to further our understanding of the coupling between the ocean and atmosphere during submarine eruptions by analyzing multiple time-series data sets, including hydroacoustic data. Only a few multiparameter observations of submarine eruptions have been made to date [Green et al. 2013; Wech et al. 2018; Tepp et al. 2020; Matoza et al. 2022]. Here, we show the value of comparing multiple data sets - including those from remotely sensed data - to elucidate the nature of volcanic activity, specifically the coupling between submarine processes and atmospheric activity for shallow submarine eruptions.

2 Fukutoku-Oka-no-Ba

FOB is located 1300 km south of Tokyo in the Ogasawara Islands, where subduction of the Pacific Plate beneath the Philippine Sea Plate causes volcanism. FOB is a conical volcano with a flat oval top (1.7 km x 1.2 km) and a vent depth of ~40 meters below sea level before the 2021 eruption, as determined with 2010 bathymetry [Otani et al. 2006; Ito et al. 2011]. Before the 2021 eruption, a minimum of seven eruptions had occurred at FOB in the last century [Japan Meteorological Agency, 2013]. These eruptions produced large pumice rafts, temporary islands that were later eroded, discolored water, and weak aerial plumes that rose to 3 km [Wakimizu 1908; Kuno 1962; Furukawa 1992; Urai 2014].

The timing, products, and impacts of the August 2021 eruption of FOB have been well characterized. The eruption started to produce a visible atmospheric plume on 12 August 2021 at 21:00 UTC [Maeno et al. 2022; Fauria et al. 2023]. The bright white and water-rich plume quickly reached 16 km asl, the height of the tropopause, and became highly elongated to the west due to the wind. Although the plume was most vigorous for the first ~14 hours of the eruption, the eruption continued through at least August 15, during which time it produced a ~0.1 km^3 floating pumice raft and a pair of new 53 million m^3 islands [Maeno et al. 2022; Fauria et al. 2023]. Over its duration, the eruption generally proceeded from vigorous and steady to weak and unsteady, with four formal phases defined by Maeno et al. [2022].

The FOB pumice raft drifted westward over 1300 km and arrived in the Okinawa prefecture of Japan, beginning two months after the eruption [e.g., Yoshida et al. 2022, among others]. Once nearshore, the pumice caused significant damage to the fishing and tourism industries by clogging ports and damaging vessels [Ohno et al. 2022]. Sampling of the FOB raft demonstrated that the clasts were of trachytic composition with glass compositions up to 68% SiO_2, although there was variation in clast color between primarily black and grey [Yoshida et al. 2022].

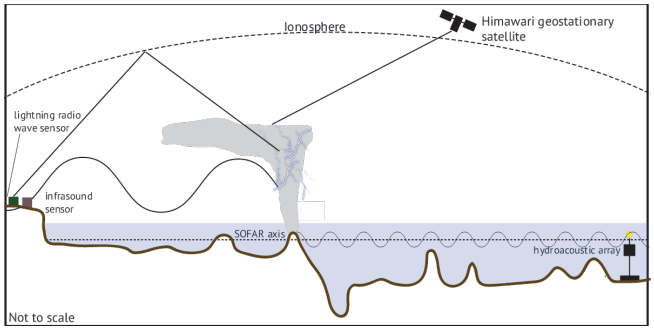

Figure 1: Schematic of remote observational sensors, including a moored hydroacoustic array, Himawari geostationary satellite, IMS infrasound array, and GLD360 lightning network.

Tani et al. [2022] conducted rapid response seafloor surveys and sampled submarine FOB deposits with remotely operated vehicles and box corers in April and August 2022. These surveys revealed little post-eruption bathymetric change [Tani et al. 2022]. The seafloor was, however, blanketed with centimeters-thick pumiceous sand, with a notable absence of pumice clasts from the raft [Tani et al. 2022].

3 Data

Because our approach relies on the analysis and correlation of multiple independent data sets from the ocean and atmosphere (Figure 1), we first describe our data sources. All our data are from remote observations, and the data types are hydroacoustic data, Himawari-8 infrared satellite observations, global lightning data, infrasound data, and atmospheric conditions.

3.1 Hydroacoustic and Infrasound array data

Our acoustic array data are from the Comprehensive Nuclear-Test-Ban Treaty Organization's (CTBTO) International Monitoring System (IMS). Figure 2 shows the locations of the Wake Island Hydroacoustic Site (H11) and infrasound (IS30 and IS39) arrays (IS45, Russia also detected the FOB eruption). H11 is a pair of 3-element arrays, north, H11N, and south, H11S, of Wake Island, USA. The triplets are outfitted with HiTec 1-100Hz hydrophones and dataloggers at each array, and sample the wavefield at 250 samples per second (sps). The geodesic distance from FOB to H11S is approximately 2688 km, giving a travel time from source to receiver of ~30 minutes at 1.5 km/s. Both arrays detected the eruption, and the data can be retrieved through the Earthscope Consortium Data Management Center. The path from FOB to the southern triplet, H11S, has fewer obstructions; therefore, we focus our analysis on its data. There is another hydroacoustic array in the Pacific, H03, off the west coast of Chile. We do not

examine the data from this array as the CTBTO Reviewed Events Bulletin (REB) did not report detections at this array.

The infrasound arrays, IS30 in Japan and IS39 in Palau, sample atmospheric pressure at 20 sps. IS30 is a 6-element array 1228 km almost due north of FOB. The travel time between FOB and IS30 is approximately 70 minutes, assuming a stratospheric propagation speed of ~0.3 km/s. The array in Palau, IS39, is south-southwest of FOB and 1995 km away. Again, assuming a stratospheric arrival, the travel time from source to array is about 115 minutes. Five of the eight array elements were operational during the eruption. We focus our infrasound analysis on data from IS39, as it had the most comprehensive record of the eruption, likely due to more favorable propagation conditions than at IS30 and IS45.

3.2 Satellite Observations

Satellite remote sensing observations are critical for observing and characterizing volcanic plumes. Maeno et al. [2022] and Fauria et al. [2023] illustrated that the Himawari-8 satellite captured a series of images of the FOB eruption. We used 12.4-micron wavelength (Band 15) infrared images available every 10 minutes. The first image of the plume occurred on 12 August 2021 at 21:10 UTC, and the last image we used was on 15 August 2021 at 15:10 UTC. We use these images, after accounting for parallax, to measure the plume dimensions (height, width, and length) and estimate the volume flux and mass eruption rate.

3.3 Global Lightning Dataset

Volcanic lightning observations are increasingly used by volcano observatories and researchers for eruption detection and characterization, respectively [Van Eaton et al. 2016; Coombs et al. 2018; Perttu et al. 2020; Van Eaton et al. 2020; McKee et al. 2021a; b; Smith et al. 2022; Perttu et al. 2023; Van Eaton et al. 2023]. We use the GLD360 lightning data product from Vaisala, Inc. [Said et al. 2013]. Vaisala's global lightning detection network is sensitive to very low-frequency (VLF, 3 to 30 kHz) electromagnetic waves emitted by lightning, which are detectable up to 10,000 km away. For each stroke, the data include the date, time (to the nearest millisecond), latitude, longitude, polarity, signal strength in kiloamperes, and an intracloud or cloud-to-ground classification. Our lightning catalog includes strokes within 50 km of FOB. We did not remove any strokes from the catalog or extend the search radius, as they were located near the vent (7.4 km mean distance and 6.7 km median distance from the vent).

3.4 Atmospheric Data

Atmospheric conditions are essential for estimating infrasonic travel times and plume volume flux. We use the ground-2-space (G2S) model [Drob et al. 2003; 2010; Drob 2019] for this study. The G2S model describes the atmosphere from 0 to 150 km above sea level (ASL) and is made available by the National Center for Physical Acoustics (NCPA) [Hetzer et al. 2024]. A series of data and models is used to compile the G2S model. The National Oceanic and Atmospheric Administration's (NOAA) Global Forecast System (GFS) model (troposphere), MERRA2 data (middle atmosphere), and in the mesosphere-thermosphere the mass spectrometer incoherent scatter radar (MSIS-00) semiempirical and the Horizontal Wind Models are input to generate the profiles [Picone et al. 2002; Rienecker et al. 2008; Bosilovich et al. 2015; Drob et al. 2015; National Centers for Environmental Prediction/National Weather Service/NOAA/U S. Department of Commerce 2015]. They include temperature, U and V wind components (eastward and northward wind velocities), density, and pressure at 0.1 km increments. We pulled atmospheric profiles at FOB every 4 hours from 12 August 2021 at 00:00 UTC to 16 August 2021 at 00:00 UTC.

4 Methods

Here, we describe how we process the data sets from Section 3.

4.1 Hydroacoustic and Infrasonic Observations

Acoustic waves travel in waveguides through the water and atmosphere [Dziak et al. 2012; Waxler et al. 2017; Dziak et al. 2023]. These waves can be detected and characterized hundreds to thousands of kilometers from their source using data recorded on arrays [Le Pichon et al. 2013]. There are many sources of noise and clutter (signals of the same type from different sources, such as another volcano erupting) in acoustic data, such as whales, earthquakes, ocean noise, wind, storms, other volcanic eruptions, and anthropogenic activity. We use

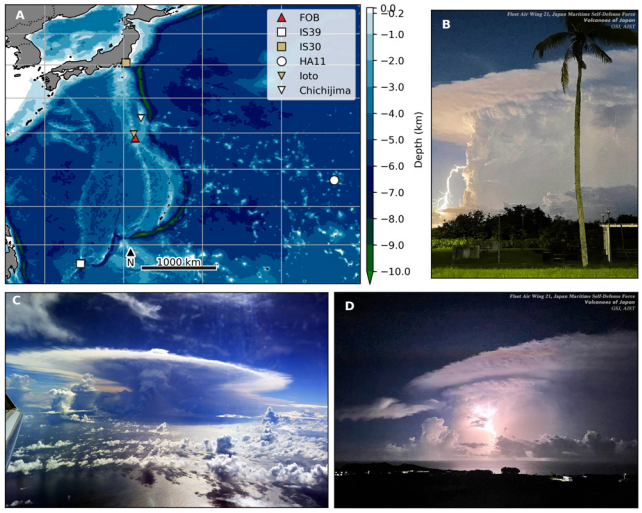

Figure 2: A) Map showing Fukutoku-Okano-Ba on the Izu-Bonin Arc south of the main four islands of Japan (red triangle), as well as the H11 hydroacoustic (white circle) and infrasonic (squares) arrays in the western Pacific region. B) Photograph taken on 13 August 2021 at ~9:00 UTC from Iwo Jima, about 60 km north of FOB. Photo courtesy of Fleet Air Wing 21, Maritime Self-Defense Force. C) A photograph of the FOB plume taken on 13 August between 06:00 and 06:30 UTC from approximately 90 km northeast at an altitude of about 6 km by the Third Regional Coast Guard Headquarters of Japan. D) Another image taken from Iwo Jima, this photograph was taken on 13 August 2021 at 10:45 UTC. Photo courtesy of Fleet Air Wing 21, Maritime Self-Defense Force.

array processing techniques to look at coherent waveforms from a specific source direction, excluding many familiar noise sources. We use the Median Cross-Correlation Maxima (Md-CCM) method [Lee et al. 2013] with weighted least squares estimation of plane wave arrival [Olson and Szuberla 2008] (Hydroacoustic) and with Least Trimmed Squares (LTS) estimator [Bishop et al. 2020] (Infrasound). In this method, we cross-correlate each unique data pair from the array elements and find the median of the maximum cross-correlation values and their corresponding time lags. Then, we use those time lags for the time-difference-of-arrival calculation. We use the data from all three hydroacoustic array elements, as three is the minimum number of data streams to estimate a unique back-azimuth and trace velocity. We apply the LTS estimator for the infrasound data, which is valuable when data channels have poor data quality or gaps. The LTS estimator can only be applied to arrays with four or more elements and is therefore a tool we can use with the infrasound data, but not the hydroacoustic data. For the hydroacoustic array processing, we filter the data between 4 and 8 Hz as Metz (2022) did and use a 10-second window with 50% overlap. We filter the infrasound data between 0.07 and 2 Hz and use an 80-second window with 90% overlap. A detection is a window of data with a median cross-correlation value of 0.7 or greater, a back-azimuth within 10 degrees of the great-circle path, and a trace velocity within a specific range, 1.43 to 1.55 km/s for hydroacoustic and 300 to 350 m/s for infrasound.

We utilized existing propagation modeling tools to constrain the hydroacoustic and infrasonic travel times. We used the PyWaveProp Python package [Lytaev 2023], which solves the Helmholtz Equation (higher-order parabolic equation) in a heterogeneous underwater environment to model the hydroacoustic propagation from FOB to H11S at 5, 10, and 50 Hz using realistic bathymetry [Ryan et al. 2009]. We used August's decadal averaged ocean sound speed for the calculations with a source at 50 m water depth and launch angles between -30 and -10 degrees (where horizontal is 0) [Affatati et al. 2022]. For the infrasound, we ran the InfraGA ray tracing code with the spherical atmosphere layer geometry [Sutherland and Bass 2004; Blom 2019; Waxler and Assink 2019; Blom and Waxler 2021]. We used the atmospheric profile from 12 August 2021 at 20:00 UTC (described in Section 3.4) and ran take off angles every 2 degrees from 20 to 50 degrees, where horizontal is zero from FOB to IS39.

4.2 Estimating Volume Flux

Volcanic plumes evolve into gravity currents that spread at an altitude of neutral buoyancy due to the density contrast between the plume material and the atmosphere. If the plume is in a strong wind field, the upwind plume will stall, and the downwind plume's speed will approach that of the wind. The FOB atmospheric plume is weak relative to the local winds and, therefore, does not expand radially. As such, we estimate the volume flux from the downwind plume spread with satellite observations using a method described by Pouget et al. [2013]. This method uses plume width measurements at distances downwind from the volcano. The volume flux from a downwind gravity current spread [Bursik et al. 1992] is

$$V = \frac{(w(x)u)^2}{2\lambda N x} \tag{1}$$

where x is some distance downwind from the vent, $w(x)$ is the measured plume width at that distance, u is the wind-speed experienced by the plume, λ is a constant of order unity, and N is the Brunt-Vaisala frequency of the atmosphere. We use $\lambda = 0.2$ based on the findings of Suzuki and Koyaguchi [2009] for tropical volcanic plumes. Figure 3 illustrates our plume width and distance from vent measurements. Figure 3A shows the plume width through time at 6 km west of the vent; the vertical dashed line in Figure 3B. Then, Figure 3C shows the length of the plume through time at the horizontal dashed line in Figure 3B. In practice, we use a threshold of 220 K; any temperatures greater than this are excluded. This eliminated any meteorological clouds within the field of view. We then count the number of pixels in each north-south column and multiply by 2 to obtain the plume width (each pixel is 2 x 2 km). The pixel above FOB is set to zero in our coordinate system. For each satellite observation, we estimate the volume flux from 2 to 200 km west of FOB.

This method assumes gravitational or density-driven and not diffuse spread. The spreading mechanism transitions from density-driven to passive transport from the vent to the downwind plume. Himawari captures the entirety of the plume, and we estimate the volume flux for each width and distance observation. However, the gravity current assumption is no longer valid at some distance; thus, the flux estimates are invalid. Costa et al. [2013] give the critical time scales at which the plume expansion regime transitions from density-driven to a combined density-driven and passive transport, t_b, and then from the combined regime to purely passive transport, t_p:

$$t_b = \frac{4\lambda N q}{9\pi u_w^2} \tag{2}$$

$$t_p = \frac{32\lambda N q}{9\pi u_w^2}, \tag{3}$$

where q is the volumetric flow rate, V from Equation 1, and u_w is the mean wind velocity. We then multiply these times by the wind speed to estimate the critical distances along the plume at which these transitions occur. We use these critical distances to note where the gravity current assumption is valid.

5 Results

To understand the connections between atmospheric and submarine processes during the 2021 FOB eruption, we compare the intensity and duration of signals measured in the ocean (hydroacoustic) with those in the atmosphere (lightning rate, infrasound, and plume width, height, and flux). We begin by introducing these observations separately. We then compare these data in time by removing the hydroacoustic and infrasonic travel times to assess their temporal correlations.

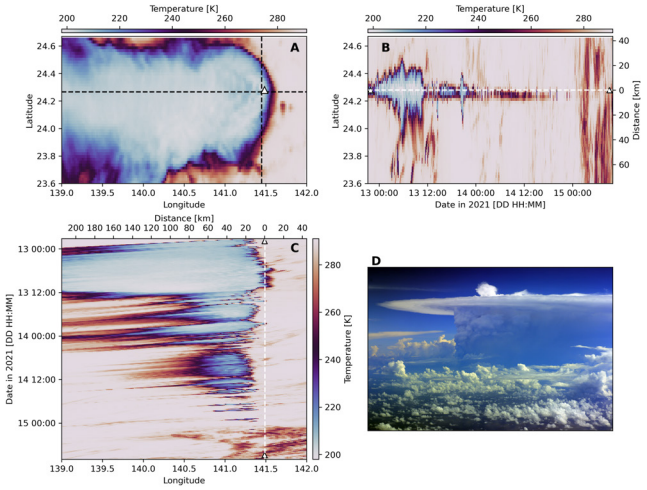

Figure 3: Fukutoku-Okano-Ba eruption plume characteristics. A) Is a snapshot of the FOB plume on 13 August 2021 at 06:00 UTC. FOB's location is the white triangle. The black dashed lines denote the plume width and length measurement positions for the time series shown in B and C. B) shows the plume width through time at the position indicated in B by the vertical black dashed line, which is 6 km west of the volcano. The white, dashed horizontal line with triangles at the ends denotes the latitudinal location of FOB. C) shows the plume length through time with the longitudinal location of FOB highlighted by the white, vertical dashed line capped by white triangles. D) A photograph of the FOB plume taken between 06:00 and 06:30 UTC from approximately 90 km northeast at an altitude of about 6 km by the Third Regional Coast Guard Headquarters of Japan.

5.1 Hydroacoustic Observations

Hydroacoustic arrays record seismo-acoustic signals in the water column. The most comprehensive observations of the FOB eruption in August 2021 are from the hydroacoustic recordings on the H11S array to the south of Wake Island, USA. Array processing results are provided in the Supplemental Information (Supp. Fig. 1). Figure 4 shows the beam from the recordings from the three array elements (A), the spectral content (B), and the number of detections per two minutes with the RMS amplitude (C). All reported signals come from the direction of FOB. A high detection rate means a consistent and highly correlated signal coming from FOB's back azimuth and having a high cross-correlation across the three elements of the Wake Island array. However, the number of detections does not directly represent the number of unique explosions at the FOB vent. A 10s window used for the beamforming data analysis can have multiple distinct and overlapping events. Furthermore, changing the window length for the data analysis (e.g., from 10 s to 30 s) or using a slightly different MdCCM threshold (e.g., from 0.7 to 0.6) can significantly change the number of detections. However, we find that the temporal pattern of detections, aggregated in 2-minute windows, is an extremely robust feature and is not dependent on our exact algorithmic choices (e.g., window length, window overlap, MdCCM threshold). Supporting Figures 14-21 show array processing results with a similar temporal pattern of detections using different combinations of window length, window overlap, and filtering band limits. The RMS amplitude is a measure of the intensity of the hydroacoustic signal.

The first detection was on 12 August 2021 at 21:07 UTC at the array, translating to a source time of 20:37 UTC as the travel time is approximately 30 minutes. The remaining times have the travel time removed. There are a few short-duration (10-40 s) signals from FOB. Then, at 20:54 UTC, the detection rate increases, the signal's spectral content broadens to 3 to 100 Hz for about 5 minutes, and then narrows to 3 to 11 Hz until 13 August 2021 at ~9:00 UTC. From then on, the detection rate is low (less than 8 per 2 minutes a third of the maximum, 24 detections per 2 minutes) for several hours. On 13 August, from ~15:00 to ~18:00, the detection rate is low to moderate (8 to 16 detections per 2 minutes), with some short periods of detection rates reaching 20 per 2 minutes. The detection rate then is high (greater than 16 per 2 minutes) for about 2 hours (~20:00 to ~22:00). From 13 August at ~22:00 to 14 August at ~11:00 the detection rate is low a few short periods where the rate is above 16 detections per 2 minutes between 00:00 and 03:00 on the 14th. Then, on 14 August, from ~11:00 to ~12:30, the detection rate is high again. From ~12:30 on 14 August to the last detection, the rate is low to zero with brief episodes of moderate to high detection rates. The high detection rate episodes late on 13 August and midday on 14 August have frequency contents similar to the sustained peak of the eruption (3-11 Hz), with higher frequencies excited for brief periods as at the eruption onset. The last hydroacoustic detection was on 15 August 2021 at 7:59 UTC.

5.2 Infrasound Observations

Multiple infrasound arrays detected the eruption (IS30, IS39, and IS44) as reported in the CTBT Reviewed Event Bulletin (REB). We processed the data from IS30 and IS39 (Supp. Figs. 2 and 3), the two closest arrays. IS30 detected only the beginning of the eruption, whereas IS39 captured more of it. Unfortunately, the IS39 observations of this eruption are limited due to high daytime wind noise and not ideal propagation paths. However, the infrasound detections provide observations of the eruption transitioning to and from subaerial. The first infrasound detection was on 12 August 2021 at 20:54 UTC. The detections decrease and become intermittent within a few hours of the eruption onset, likely due to wind noise. Figure 5A shows the infrasound waveform with those detected from FOB in blue. At the bottom of A, the light and dark blue bars denote daytime and nighttime at the IS39 array, respectively. In Figure 5, on 12 August at ~22:30 UTC the waveform amplitude increases (A), the spectrogram shows a high power at low frequencies (B), and the detection rate decreases (C) during the daytime. Then, the detection rate is moderate to high again on 13 August at ~4:00 UTC and high at night when the noise is low, ~ 11:00 UTC. This repeats on the next two days. The last infrasound detection was on 15 August 2021 at 05:05 UTC. Atmospheric conditions suggest a thermospheric guide and propagation modeling finds a celerity of 260 m/s (Supp. Figure 10); however, this does not match regional observations [Maeno et al. 2022]. A celerity of 280 m/s matches

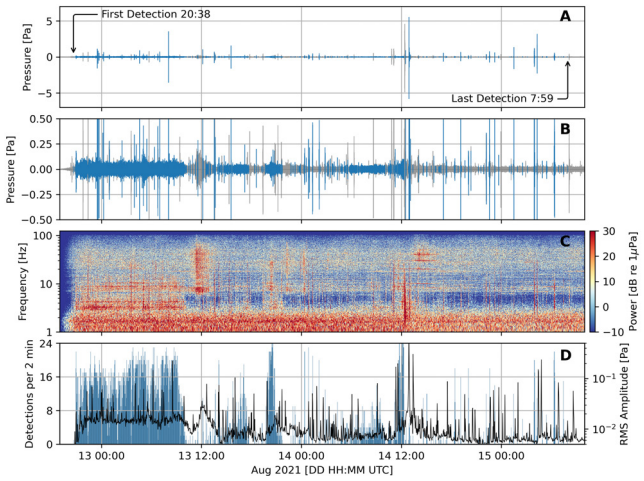

Figure 4: H11S hydroacoustic data from the FOB eruption. A) shows the hydroacoustic beam from the three-element array data. The beam is blue for times when there are detections from the eruption. B) shows the same as A, with the higher amplitudes clipped to show details of the lower amplitude data. C) shows the spectrogram for the beam. D) shows the number of detections per 2-minute window of data. We removed the travel time and show time at the source (FOB). The maximum number of detections in two minutes is 24, given the array processing parameters (10-second window with 50% overlap). The black line is the RMS amplitude of the beam using a 5-minute window.

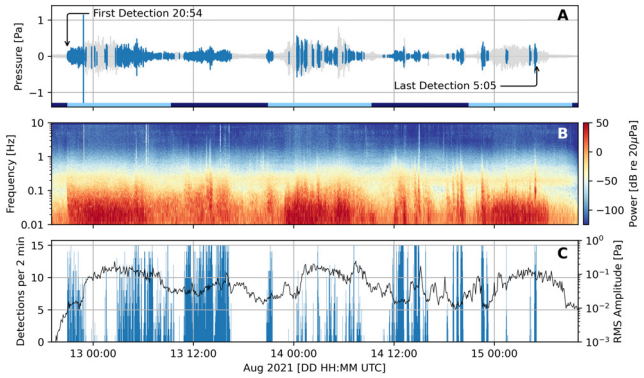

Figure 5: IS39 infrasonic data from the FOB eruption. A) shows the infrasound beam from the IS39 array data. The beam is blue for times when there are detections from the eruption. The light and dark blue line shows the array's local day and nighttime. B) shows the spectrogram for the beam. C) shows the number of detections per 2-minute window of data. The maximum number of detections in two minutes is 15, given the array processing parameters (80-second window with 90% overlap). We removed the travel time and show time at the source (FOB). The black line is the RMS amplitude of the beam using a 5-minute window.

the onset time from Maeno et al. [2022] and aligns with an intensification on the hydroacoustic time series.

5.3 Lightning Observations

The Fukutoku Oka-no-Ba eruption was lightning-rich [Fauria et al. 2023]. Figure 6 shows the lightning at FOB detected by the GLD360 network through time. The first stroke was detected on 12 August 2021 at 21:09:15 UTC, and the last on 14 August 2021 at 22:57:51 UTC. During those ~44 hours, 136,160 strokes were recorded. This is about a quarter of the strokes observed by GLD360 for the Hunga eruption, over about 4 times as many hours [Van Eaton et al. 2023]. Figure 6A is a stacked histogram showing the contribution of intracloud (black) and cloud-to-ground (orange) stroke rates to the total. The lightning locations are distributed around FOB, with slightly more to the west. The stroke rate for the first few hours of the eruption is 50-100+ strokes per minute (SPM). Then, from 12 Aug 2021 at 22:00 UTC to 13 August 2021 at 11:00 UTC, the stroke rate increases and remains elevated at 100 to 200+ SPM. The stroke rate ranges from 0 to 200+ SPM on 13 August from ~11:00 to ~19:00 Figure 6A. On 13 August from ~19:30 to ~22:00 we observe the highest stroke rate, reaching 300 SPM (Figure 6D). There are two pulses (14 August at ~01:00 and ~13:00) where the stroke rate reaches 200+ SPM; otherwise, the rates max out around 100 SPM. From ~12:00 on 14 August, the time between lightning pulses increases until the last detection at 22:58.

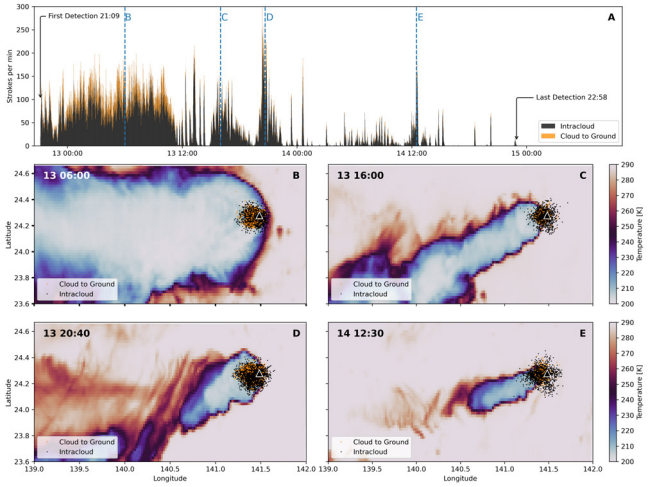

Figure 6: Lightning during the FOB eruption. A) shows the lightning detections per minute in a stacked histogram. The black is the intracloud (lightning within the plume), and the orange is cloud-to-ground lightning strokes. B-E) show lightning locations within 20 minutes of the plume observation displayed.

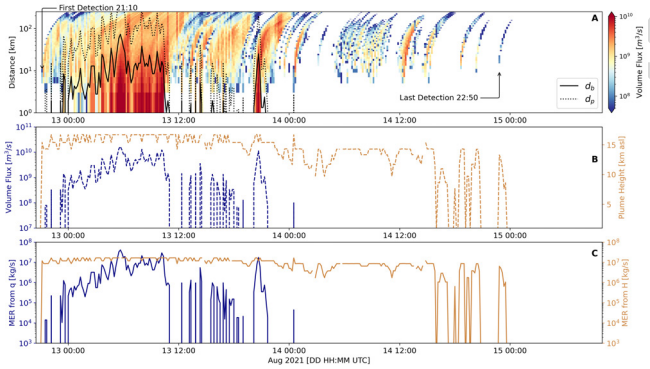

Figure 7: FOB Plume Volume Flux. A) Plume volume flux with time and distance. The solid black line denotes the boundary between density-driven flow and mixed density-driven and passive transport. The dotted black line marks the boundary between mixed density-driven and passive transport and purely passive transport. B) is volume flux using plume width measurements 6 km west of FOB (dashed navy line), and the dashed dark orange is the maximum plume height from Fauria et al. [2023]. C) shows the mass eruption rate estimated from the volume flux (navy line) and maximum plume height (dark orange) shown in B.

5.4 Plume Observations and Volume Flux Estimates

The Himawari-8 satellite captured the plume starting on 12 August 2021 at 21:10 UTC. For each Himawari-8 observation, we measured the plume width along a 270-degree azimuth at 2-kilometer intervals from the vent and used these measurements to compute a volume flux estimate (Section 4.2, Equation 1). The plume widths range from 2 km to 136 km. The maximum plume width within 10 km of the vent was 50 km. We have volume-flux estimates from 2 to 200 km from the vent, depending on the plume extent. These results are shown in Figure 7A. The volume flux values range from 10^7 to 10^9 m^3/s. The maximum volume flux is 1.7 $x10^{10}$ m^3/s on 13 August at 5:30 UTC (4.1 x 10^7 kg/s). From 12 August at ~23:00, the flux gradually increases until the maximum and then stays elevated until about 09:00 on 13 August. The flux is then lower and intermittent until 13 August at ~20:00, when the flux increases to 10^9 m^3/s for an hour. Then, the volume flux is lower, and the plume is less continuous/pulsatory. The last plume observation is at 22:50 on 14 August 2021. Figure 7B and C show the volume flux and mass eruption rate (MER) estimates at a horizontal distance of 6 km west of FOB in blue. The orange lines show the maximum plume height from Fauria et al. [2023] and the MERs estimated from those heights. The MER derived from volume flux exhibits greater variability than the MER estimated from plume height. Also included in Figure 7A are our critical distances denoting the transition from density-driven to a combined regime, d_b, solid black line, and combined to passive transport, d_p, dotted black line. These critical distance estimates indicate that many volume flux measurements correspond to a combined regime or to a passively transported plume. During the peak of the eruption early on 13 August and later that same day at ~20:00 UTC, the critical distances highlight the transition from density-driven to a combined regime, and then to passive transport. The low number of volume flux estimates that satisfy the gravity-current assumption suggests that most of our volume fluxes are underestimated.

5.5 Cross-correlation analyses

We compute cross-correlations to assess the similarity among the lightning, hydroacoustic, and volume-flux time series. The hydroacoustic data have the travel time removed. When correlating the lightning and hydroacoustic detections per 2 minutes, we obtain a Pearson correlation coefficient (PCC) of 0.81, indicating that the two are highly correlated in time (Supp. Fig. 4). A correlation coefficient of 1 is perfect, 0 is uncorrelated, and we consider a correlation coefficient above 0.7 to be strongly or highly correlated. This cross-correlation analysis yields a peak correlation coefficient at a lag of 720 s, indicating that hydroacoustic detections precede lightning detections. We cross-correlated the lightning detections per 10 minutes with the volume flux data, yielding a PCC of 0.82, with the volume flux lagging by 10 minutes (Supp. Fig. 5). We use a coarser detection per time interval (10 versus 2 minutes) in cross-correlating the volume flux because we only have a volume flux data point every 10 minutes. Correlating the hydroacoustic detections per 10 minutes with the volume flux yields a PCC of 0.73 with a 20-minute lag (Supp. Fig. 6). We also cross-correlated the hydroacoustic RMS amplitude data with the lightning detection rate and the volume flux. These correlations yielded low PCCs: 0.38 and 0.41, respectively. Lastly, we cross-correlated the infrasound detections with the hydroacoustic detections, lightning detections, and volume flux, yielding PCCs of 0.64, 0.62, and 0.61, respectively, and lags of 450, 340, and 340 minutes, respectively. While these PCCs indicate moderate correlation, the associated lags shift the infrasound to prior to the start of the eruption, which is unrealistic.

6 Discussion

We observe strong temporal correlations among the lightning, hydroacoustic, and plume-derived flux data (Figure 8). Below, we explore how and why flux at the vent can be responsible for the timing and intensity of both the lightning and hydroacoustic data. We, therefore, argue that these geophysical signals are correlated and caused by a common process - eruptive intensity at the vent. Our discussion assumes that volume flux, as derived by Eq. 1, can be fundamentally related to flux at the vent for this eruption.

6.1 Processes recorded by hydroacoustic data

The hydroacoustic data in Figure 4 show when the FOB eruption produces sound well coupled to the water column. Processes at submarine volcanic vents that produce sound include discrete or continuous explosive and mass-wasting processes [Tepp and Dziak 2021]. The spectral content of FOB's hydroacoustic data (3-11 Hz, sometimes up to 100 Hz) is similar to the 2010 South Sarigan (2-10 Hz, sometimes up to 50 Hz) [Green et al. 2013] or 2009 (<20 Hz) and 2022 (<10 Hz) Hunga [Bohnenstiehl et al. 2013; Le Bras et al. 2022] eruptions. The South Sarigan and 2022 Hunga eruptions were recorded remotely at 1000+ km, similar to FOB, and the 2009 Hunga eruption was recorded regionally at 150 km. The frequency content of these remotely observed eruptions reflects the source's size (the larger the source, the lower the frequency) and the efficiency of low-frequency sound to propagate in seawater [Jensen et al. 2011]. The long and mostly continuous duration of the hydroacoustic signals suggests that the vent was fully submerged, such that the signals coupled well into the water column throughout the eruption.

From the eruption onset, the hydroacoustic data correlate well with flux in the atmospheric plume and lightning stroke rate (Figure 8). These correlations lead us to believe that the FOB hydroacoustic signals are driven directly by the eruptive processes at the vent, such as jetting or explosions, which also directly impact the atmospheric volcanic column.

Beyond August 15, 00:00 UTC, we observe hydroacoustic signals without accompanying lightning or volume flux signals. We interpret these as small and/or discrete explosions that were not energetic enough to generate a subaerial plume detectable by satellites or significant lightning. Alternatively, the hydroacoustic signals on August 15 and beyond could be caused by small mass-wasting events that do not affect the atmosphere. However, a video taken by the Japan Coast Guard at 3:10 UTC on 15 August shows one of these explosive events that breached the ocean surface but was too small to be seen in satellite imagery (Figure 8C) of this event. We therefore conclude that the hydroacoustic signals beyond 15 August also record smaller explosions at the vent.

Although we lack a quantitative relation between recorded sound and eruptive processes in water, we argue that the FOB hydroacoustic detection rate and intensity can be related to eruptive flux, as the hydroacoustic detection rate correlates with volume flux (PCC of 0.73). Data sets such as those reported here may be foundational for establishing more quantitative relationships between sound and flux. For example, quantitative models exist for the sound generated by the expansion and burst of singular bubbles [Li et al. 2021; Liu et al. 2021; Roche et al. 2022]. Sustained eruptions generate a more complex source of sound. However, future work may investigate how much the sound generated by eruptions such as FOB fits a jetting model where a Strouhal number describes the relationship between frequency content, vent diameter, and velocity as found in subaerial acoustics [e.g., Tam et al. 2008; Matoza et al. 2009; 2013; Matheus et al. 2021, among others].

6.2 Processes recorded by the lightning data

The lightning stroke rate is highly similar to the hydroacoustic detection rate and volume flux (Figure 8). Lightning fundamentally results from charge separation in volcanic plumes, which is driven by particle fragmentation and collision [Mather and Harrison 2006; Cimarelli et al. 2022]. Particle collisions include ash-ash collisions lower in the plume and ice-ice collisions, including ice-covered ash, above the -20°C isotherm [Dickinson et al. 1981; Aplin et al. 2014; Méndez Harper and Dufek 2016]. While large amounts of external water have been shown to depress charging lower in a plume, it seems to enhance electrification above the local ice nucleation level in the atmosphere [Genareau et al. 2018; Maters et al. 2019; 2020]. Modeling that incorporated microphysics suggests surface water interaction influences column stability and highlights how surface water can be incorporated and jettisoned to the stratosphere [Van Eaton et al. 2012]. Turbu-

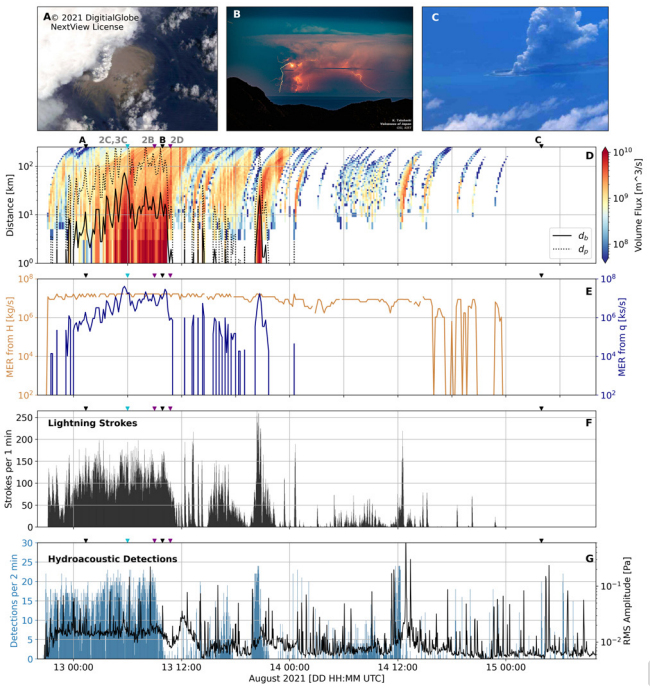

Figure 8: Comparison of FOB observations with images of the eruption. A) shows the aerial plume and pumice raft on 13 Aug 2021 01:22 UTC. Image is ©2021, DigitalGlobe, Inc., a Maxar company; NextView License. B) is a photograph taken on 13 August 2021 at 9:53 UTC from Chichijima, about 320 km NNE of FOB. Photo by K. Takahashi. C) is an image taken on 15 August at 3:56 UTC. Photo credit: Japan Coast Guard and JMA. The inverted black triangles at the top of D-G show when images A-C were taken. The inverted cyan triangles denote when images Figure 2C and Figure 3C were captured. The inverted purple triangles denote when images Figure 2B and Figure 2D were taken. D-E) shows the plume volume flux and MER as in Figure 7. F) shows the lightning strokes per minute as in Figure 6 without distinguishing between intracloud and cloud-to-ground strokes. G) shows the hydroacoustic detection rate and RMS amplitude of the beam.

lence plays a role in particle distribution and collisions, leading to particle separation and lightning [Behnke et al. 2013; Cimarelli et al. 2022; Ichihara et al. 2023]. Because larger, higher-flux columns are more turbulent, increasing turbulence increases particle-particle interactions and sorting for charge separation; the volume flux likely exerts first-order control on lightning generation. Recent studies suggest a relationship between plume parameters (height, radius, and flux) [Smith et al. 2021; Van Eaton et al. 2022; Ichihara et al. 2023]. We also conclude that the flux into the eruption column determines the lightning stroke rate at FOB. Therefore, lightning and hydroacoustic detection rates correlate because both are products of eruptive flux.

6.3 Observations of eruption onset and cessation

At FOB, the observations at the onset are sequential, likely reflecting the eruption intensifying and the plume rising to above the -20°C isotherm where ice nucleates, providing an additional charging mechanism for lightning generation. Figure 9 shows the first hours of the eruption, and Table 1 lists times and observations. Hydroacoustic signals begin on 12 August at 20:38 UTC and intensify ~16 minutes later at 20:54 UTC. When the hydroacoustic signal intensifies, the infrasound signal begins. Our constraint of the subaerial eruption onset with remote infrasound agrees with previous characterizations with regional infrasound and satellite observations [Maeno et al. 2022; Fauria et al. 2023]. Then, at ~21:09 UTC, the lightning detections begin, and the following Himawari-8 image captures a plume at 21:10 UTC. There is a 15-minute delay between the eruption becoming subaerial at 20:54 (i.e., hydroacoustic intensification and infrasound onset) and the first lightning detection. By cross-correlating the lightning detections, the hydroacoustic detections, and the volume flux, we found that the lightning detections lag the hydroacoustic detections by 720 s (12 minutes), and the volume flux lags the hydroacoustic detections by 20 minutes and the lightning detections by 10 minutes. This 12-15 minute delay is consistent with the time a plume can take to rise into the atmosphere far enough for volcanogenic ice nucleation [Cimarelli et al. 2022]. From 21:00 to 21:10 UTC on 12 August 2021, the plume height increased from undetectable to 15 km asl. 15 km in 10 minutes gives a rise speed of 25 m/s. The -20°C isotherm was at 8.4 km asl. Given this rise speed estimated from the Himawari-8 observations, the plume would take 5-6 minutes to rise above the -20°C isotherm. There may have been lightning earlier that was not detectable. Vaisala's global lightning detection network is sensitive to lightning that generates VLF electromagnetic waves. As the frequency is inversely related to stroke length, the smaller strokes that generate higher-frequency electromagnetic waves are only detectable with local instrumentation. An increase or delay in lightning detections until after a plume rises above the -20°C

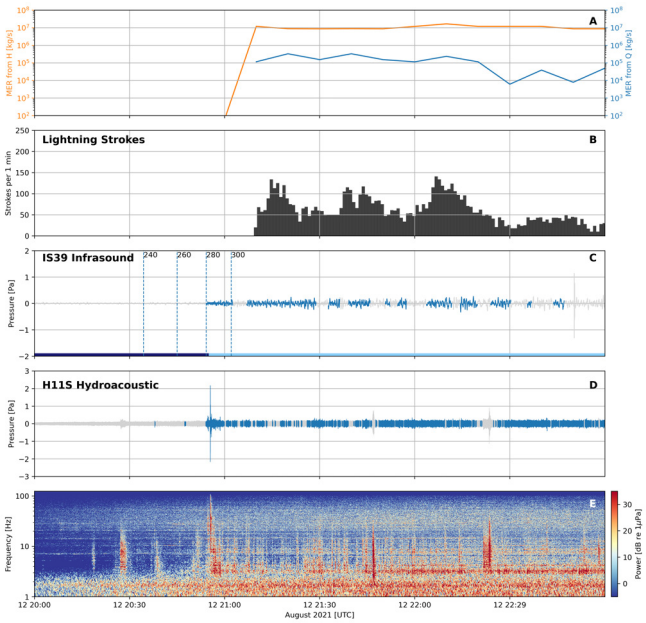

Figure 9: The first hours of the eruption. A) Shows the MER from plume height and volume flux. B) Shows lightning rate per minute. C) Show IS39 infrasound beamform with sound from FOB plotted in blue. The vertical dashed lines show thermospheric celerities from 240 to 300 m/s. D) Hydroacoustic beamform with sound from FOB in blue. E) Spectrogram of Hydroacoustic data.

isotherm has been observed during other eruptions [Arason et al. 2011; Behnke et al. 2013; Van Eaton et al. 2016; Prata et al. 2020; Van Eaton et al. 2020]. An alternative interpretation is that lightning strokes make contact with water, thereby directly triggering the hydroacoustic signals [Hill 1985]. We do not favor this alternative hypothesis, partly because Figure 6A shows that most lightning strokes do not make ground (or ocean) contact (78% are intracloud and 22% are cloud-to-ground).

Table 1: Summary of eruption onset and cessation sequences.

2021 [UTC]	Observation
08-12 20:38	First hydroacoustic detection - the start of the detectable subaqueous activity
08-12 20:54	Hydroacoustic detection rate increases to near-continuous with increased RMS amplitude
08-12 20:54	First infrasonic detection, eruption has breached the ocean surface - Remotely detectable sub-aerial activity begins
08-12 21:09	First lightning detection - the start of globally detectable lightning
08-12 21:10	First plume detection
08-14 22:50	Last plume detection
08-14 22:58	Last lightning detection - the end of globally detectable lightning
08-15 05:05	Last infrasound detection - end of detectable subaerial activity
08-15 07:59	Last hydroacoustic detection - end of detectable subaqueous activity

6.4 Event identification and classification

Event identification and classification (EIC) is a classic and evolving problem in seismo-acoustic data that takes different forms depending on a given individual's definition of a signal versus noise. Simply put, the aim is to identify event start time, duration, source location, and frequency content of individual events and classify them into distinct classes, typically with specific underlying physical processes. In volcano seismo-acoustics, observatories have developed classification schemes based on local seismic network observations [Minakami 1960; Latter 1979], and these schemes typically reflect the technology of the time. Recent review papers have nicely illustrated seismic [McNutt and Roman 2015], infrasonic [Fee and Matoza 2013], and hydroacoustic [Tepp and Dziak 2021] event types. The nuances of EIC algorithms are also different for instruments deployed as a network versus an array. In this study of FOB, we utilized array data and applied the MdCCM arraying processing tool, which outputs detections—i.e., time windows wherein the signal's azimuth is consistent with FOB's locations. However, individual detections do not directly translate to events such as the number of volcanic explosions. Instead, a list of detections is a step toward identifying events. Events in volcano seismo-acoustics include but are not limited to earthquakes, explosions, landslides, lahars, jetting, sustained eruptions, long-period events, very-long-period events, and tremor. These events have different frequency content, impulsivity, and durations. With the array processing tool we applied to the hydroacoustic data (and is typically used in other similar analyses), a detection is a 10-second window of data that has passed three criteria: a median cross-correlation maximum value of 0.7 or higher, a trace velocity within 1430 to 1530 m/s, and a back-azimuth of 288±5°. We use a window overlap of 50%. With this strategy, an explosion lasting 60 seconds, which we would consider a single event from a physical perspective, would have 12 associated detections. The ratio of detections to events is 1:1 for event durations less than or equal to and completely contained within the detection window with 0% overlap. As event durations and

percent overlap increase, the ratio increases. A large eruption with a sustained jet flow lasting several hours could be considered a single event, with hundreds to thousands of detections, depending on the window length and percentage of overlap. Thus, we would urge caution in directly interpreting the number of detections from seismo-acoustic array processing as individual "events" without further processing and careful waveform analysis.

One potential mechanism to classify individual events/detections is the signal's frequency content. Higher frequencies attenuate at regional and remote observational distances, and path effects complicate signals (Supp. Figures 11, 12, 13). Tanaka et al. [2025] take on the challenging task of distinguishing volcanic eruption versus volcano-tectonic earthquake signals in hydroacoustic array data. They detect events with semblance (a similar conceptual approach to our method) and use a frequency index to classify detections as either volcanic eruptions or volcano-tectonic earthquakes. Their index considers the relative importance of high (25-50 Hz) vs low (5-15 Hz) frequency content in the detections' waveforms. They note that volcanic eruptions contain these high frequencies, and tectonic earthquakes (T-phases) have dominant frequencies below 15 Hz. The results of the frequency index classification technique suggest the hydroacoustic signal from FOB starts as eruptive and then alternates between eruptive and volcano-tectonic earthquake signals. In Figure 9E at 20:54, the event excites frequencies from 3 to 100 Hz, and then the eruption shifts to 3 to 11 Hz. Our examination of this same period of the eruption (Figure 9) suggests the hydroacoustic signal is primarily eruptive, given the complementary infrasound, lightning, and plume observations. At approximately 22:20 in Figure 9, there is an earthquake with frequency content similar to FOB detections that array processing indicates has a high MdCCM, but it comes from a different back-azimuth (Supp. Fig. 7). Supp. Figures 8 and 9 show another example of FOB detections with frequency content similar to that of an earthquake in Alaska. Thus, we find that while signal frequency is a critical tool for characterizing hydroacoustic events, care must be taken in its interpretation and use as a simple classifier since the final frequency detected at stations 1000s of km away is affected by a number of complexities associated with long distance propagation as well as near volcano water and seafloor properties (for the initial reflections and propagations). A detailed spectral analysis of the detections is beyond the scope of the present work; however, our results could provide a valuable dataset for assessing the types of frequency signals associated with large submarine volcanism and their relationships to various source models [Aiken 2024; Lavayssière et al. 2024].

6.5 Impacts of multi-parameter remote sensing datasets

Flux is an essential parameter in eruptions. As the ERUPT NAS report emphasizes, a central goal of volcanology is to "Develop techniques to measure temporal variations in eruption rate and correlate those to variability in eruptive products" [NAS 2017]. We make strides towards that goal by measuring variations in eruptive flux and comparing them to lightning rate and hydroacoustic intensity. Often, a single flux value is assigned to an event, which can correspond to height. Here, we show how flux is variable in time even when the maximum plume height, in the case of FOB, is pinned close to the tropopause.

It is rare to have multiparameter observations of submarine eruptions that generate an atmospheric eruption column. There are only three submarine eruptions documented in the literature with plume observations from the modern geostationary constellation: 2016-2017 Bogoslof, 2020-2021 Hunga, and 2021 FOB [Schneider et al. 2020; Carr et al. 2022; Gupta et al. 2022; Maeno et al. 2022; Proud et al. 2022; Fauria et al. 2023]. Recent theoretical work explores the relationship between flux and water depth, and their impact on buoyant plume generation [Rowell et al. 2022]. Large atmospheric columns occur only for very large and/or shallow eruptions. FOB was at a shallow (~40 m) but still submarine depth where both atmospheric and submarine hydroacoustic signatures are possible. For the FOB depth and eruption rates, one would expect large plumes, possibly turbulent water mixing, and a steam source. At its peak, the FOB eruption maps onto the Rowell et al. [2022] subaerial buoyant plume region with its water depth of 40 m and maximum mass flux of 4.1 x 10^7 kg/s from the volume flux estimates. With each new generation of geostationary satellites, the spatio-temporal resolution improves, and the available spectral bands expand [Schmit et al. 2005; Hillger and Schmit 2009; Schmit et al. 2017]. With the launches of Himawari-8 in 2014, GOES-E in 2016, and GOES-W in 2017, the full-disk image rate decreased from every 15 minutes to every 10 minutes. Even with the 10-minute observation rate, there were instances when Himawari-8 observed the plume, but it was not attached to the vent. A higher satellite observation rate may allow us to capture more of the density-driven plume in the future.

7 Conclusions

A central challenge in volcanology is that we largely lack the ability to quantitatively derive eruption parameters, such as eruptive flux, from the spatiotemporal frequencies of the geophysical signals we record. In addition, although many studies have suggested that eruption characteristics and the intensity of geophysical signals are related, we have few examples that demonstrate these connections or their absence [Stix 2018; McKee et al. 2021a; b; Smith et al. 2021].

The 2021 FOB datasets show strong correlations between lightning stroke rate, hydroacoustic detection rate, and plume-derived volume flux (Figure 8). The observations at the onset are sequential from hydroacoustic to infrasonic to lightning to plume, showing a progression from subaqueous to breaching to subaerial over 30 minutes. Then, as the eruption wanes, the observations reverse, with the hydroacoustic and infrasonic observations better capturing the end of the eruption. The eruption volume flux ranges from 10^7 to 10^9 m^3/s. Volume flux is highly correlated with the hydroacoustic and lightning detection rates, suggesting the subaqueous and subaerial processes are coupled. We suggest that the high similarity reflects a common source and indicates that all three processes are driven by near-vent eruption intensity. Thus, our analysis

provides a unique and rich dataset for understanding shallow submarine eruptive dynamics and a framework for potentially relating far-field hydroacoustic data directly to eruptive fluxes.

Author Contributions

KFM: Conceptualization, Methodology, Formal analysis, Investigation, Writing-original draft, Writing-review & editing, Visualization, Project administration. **KEF**: Conceptualization, Methodology, Writing-original draft, Writing- Reviewing & Editing, Visualization, Funding acquisition. **JCA**: Conceptualization, Writing-review & editing. **JDA**: Conceptualization, Investigation, Writing-review & editing. **ML**: Conceptualization, Formal analysis, Investigation, Writing-review & editing. **TM**: Conceptualization, Formal analysis, Writing-original draft, Writing-review, & editing. **FM**: Writing- Reviewing & Editing. **MI**: Writing- Reviewing & Editing. **DM**: Writing- Reviewing & Editing. **CV**: Investigation, Writing- Reviewing & Editing.

Acknowledgements

DigitalGlobe/Maxar data were provided by the Commercial Archive Data for NASA investigators (https://cad4nasa.gsfc.nasa.gov) under the National Geospatial-Intelligence Agency's NextView license agreement. This work was funded by National Aeronautics and Space Administration grant 80NSSC20K1450 (K.F.M., K.E.F.). T.M. acknowledges support by the Packard Fellowship for Science and Engineering. We thank the Japan Meteorological Agency and Japan Coast Guard for their essential roles in responding to and documenting this eruption. We thank John Rausch for his help with accessing and using Himawari-8 data, and Ralf Bennartz for informative discussions on remote sensing science. The views expressed in this study are those of the authors and do not necessarily reflect those of the Preparatory Commission for the CTBTO. We thank three anonymous reviewers for their constructive feedback.

Data Availability

The hydroacoustic data from H11N and H11S arrays are available to download from the IRIS/Earthscope Consortium Data Management Center (https://ds.iris.edu/ds/nodes/dmc/data/). The G2S atmospheric model can be downloaded from the National Center for Physical Acoustics, the University of Mississippi (https://g2s.ncpa.olemiss.edu/). CTBT IMS infrasound network data and CTBTO Reviewed Events Bulletin (REB) are available for researchers through the vDEC program with the Comprehensive Nuclear-Test-Ban Treaty Organization (CTBTO) (https://www.ctbto.org/specials/vdec/). GLD360 data are available upon request from Vaisala Inc. JMA Himawari-8/9 imagery can be downloaded through Amazon Web Services (https://registry.opendata.aws/noaa-himawari/).

Copyright Notice

References

Affatati, A., C. Scaini, and S. Salon (2022). *Underwater sound speed and sound speed error simulations for present (2006-2016) and future (2090-2100) decades under RCP8.5 climate scenario (NCEI Accession 0244993)*. Last Modified: 2025-04-15. DOI: 10.25921/tvy2-2290.

Aiken, C. (2024). "Listening for Diverse Signals From Emergent and Submarine Volcanoes". *Geophysical Monograph Series*. Edited by G. Bayrakci and F. Klingelhoefer. 1st edition. Wiley, pages 43–58. ISBN: 978-1-119-75089-5 978-1-119-75092-5. DOI: 10.1002/9781119750925.ch4.

Aplin, K., K. Nicoll, and I. Houghton (2014). "Electrical charging of volcanic ash". *Proc ESA Annual Meeting on Electrostatics*.

Arason, P., A. J. Bennett, and L. E. Burgin (2011). "Charge mechanism of volcanic lightning revealed during the 2010 eruption of Eyjafjallajökull". *Journal of Geophysical Research* 116(2), pages 5315–5355. DOI: 10.1029/2011JB008651.

Behnke, S. A., R. J. Thomas, S. R. McNutt, D. J. Schneider, P. R. Krehbiel, W. Rison, and H. E. Edens (2013). "Observations of volcanic lightning during the 2009 eruption of Redoubt Volcano". *Journal of Volcanology and Geothermal Research* 259(C), pages 214–234. DOI: 10.1016/j.jvolgeores.2011.12.010.

Bishop, J. W., D. Fee, and C. A. L. Szuberla (2020). "Improved infrasound array processing with robust estimators". *Geophysical Journal International* 221(3), pages 2058–2074. DOI: 10.1093/gji/ggaa110.

Blom, P. (2019). "Modeling infrasonic propagation through a spherical atmospheric layer—Analysis of the stratospheric pair". *The Journal of the Acoustical Society of America* 145(4), pages 2198–2208. DOI: 10.1121/1.5096855.

Blom, P. and R. Waxler (2021). "Characteristics of thermospheric infrasound predicted using ray tracing and weakly non-linear waveform analyses". *The Journal of the Acoustical Society of America* 149(5), pages 3174–3188. DOI: 10.1121/10.0004949.

Bohnenstiehl, D. R., R. P. Dziak, H. Matsumoto, and T. .-. A. Lau (2013). "Underwater acoustic records from the March 2009 eruption of Hunga Ha'apai-Hunga Tonga volcano in the Kingdom of Tonga". *Journal of Volcanology and Geothermal Research* 249, pages 12–24. DOI: 10.1016/j.jvolgeores.2012.08.014.

Bosilovich, M. G., S. Akella, C. Lawrence, R. Cullather, C. Draper, R. Gelaro, R. Kovach, Q. Liu, A. Molod, P. Norris, K. Wargan, W. Chao, R. Reichle, L. Takacs, R. Todling, Y. Vikhliaev, S. Bloom, A. Collow, G. Partyka, G. Labow, S. Pawson, O. Reale, S. Schubert, and M. Suarez (2015). *MERRA-2: Initial Evaluation of the Climate*. Technical report NASA/TM-2015-104606/VOL.43. NTRS Author Affiliations: NASA Goddard Space Flight Center, Science Systems and Applications, Inc., Maryland Univ., Univer-

sities Space Research Association NTRS Document ID: 20160005045 NTRS Research Center: Goddard Space Flight Center (GSFC).

Bryan, G. M., M. Truchan, and J. I. Ewing (1963). "Long-Range SOFAR Studies in the South Atlantic Ocean". *The Journal of the Acoustical Society of America* 35(3), pages 273–278. DOI: 10.1121/1.1918448.

Bursik, M. I., S. N. Carey, and R. S. J. Sparks (1992). "A gravity current model for the May 18, 1980 Mount St. Helens plume". *Geophysical Research Letters* 19(16), pages 1663–1666. DOI: 10.1029/92GL01639.

Caplan-Auerbach, J., R. P. Dziak, J. Haxel, D. R. Bohnenstiehl, and C. Garcia (2017). "Explosive processes during the 2015 eruption of Axial Seamount, as recorded by seafloor hydrophones". *Geochemistry, Geophysics, Geosystems* 18(4), pages 1761–1774. DOI: 10.1002/2016GC006734.

Carr, J. L., Á. Horváth, D. L. Wu, and M. D. Friberg (2022). "Stereo Plume Height and Motion Retrievals for the Record-Setting Hunga Tonga-Hunga Ha'apai Eruption of 15 January 2022". *Geophysical Research Letters* 49(9). DOI: 10.1029/2022GL098131.

Chadwick Jr., W. W., K. V. Cashman, R. W. Embley, H. Matsumoto, R. P. Dziak, C. E. J. de Ronde, T. K. Lau, N. D. Deardorff, and S. G. Merle (2008). "Direct video and hydrophone observations of submarine explosive eruptions at NW Rota-1 volcano, Mariana arc". *Journal of Geophysical Research: Solid Earth* 113(B8). DOI: 10.1029/2007JB005215.

Chadwick Jr., W. W., S. L. Nooner, D. A. Butterfield, and M. D. Lilley (2012). "Seafloor deformation and forecasts of the April 2011 eruption at Axial Seamount". *Nature Geoscience* 5(7), pages 474–477. DOI: 10.1038/ngeo1464.

Cimarelli, C., S. Behnke, K. Genareau, J. M. Harper, and A. R. Van Eaton (2022). "Volcanic electrification: recent advances and future perspectives". *Bulletin of Volcanology* 84(8), page 78. DOI: 10.1007/s00445-022-01591-3.

Coombs, M. L., A. G. Wech, M. M. Haney, J. J. Lyons, D. J. Schneider, H. F. Schwaiger, K. L. Wallace, D. Fee, J. T. Freymueller, J. R. Schaefer, and G. Tepp (2018). "Short-Term Forecasting and Detection of Explosions During the 2016–2017 Eruption of Bogoslof Volcano, Alaska". *Frontiers in Earth Science* 6, pages 214–217. DOI: 10.3389/feart.2018.00122.

Costa, A., A. Folch, and G. Macedonio (2013). "Density-driven transport in the umbrella region of volcanic clouds: Implications for tephra dispersion models". *Geophysical Research Letters* 40(18), pages 4823–4827. DOI: 10.1002/grl.50942.

Dickinson, J. T., E. E. Donaldson, and M. K. Park (1981). "The emission of electrons and positive ions from fracture of materials". *Journal of Materials Science* 16(10), pages 2897–2908. DOI: 10.1007/BF02402856.

Drob, D. P. (2019). "Meteorology, Climatology, and Upper Atmospheric Composition for Infrasound Propagation Modeling". *Infrasound Monitoring for Atmospheric Studies: Challenges in Middle Atmosphere Dynamics and Societal Benefits*. Edited by A. Le Pichon, E. Blanc, and A. Hauchecorne. Cham: Springer International Publishing, pages 485–508. ISBN: 978-3-319-75140-5. DOI: 10.1007/978-3-319-75140-5_14.

Drob, D. P., J. T. Emmert, J. W. Meriwether, J. J. Makela, E. Doornbos, M. Conde, G. Hernandez, J. Noto, K. A. Zawdie, S. E. McDonald, J. D. Huba, and J. H. Klenzing (2015). "An update to the Horizontal Wind Model (HWM): The quiet time thermosphere". *Earth and Space Science* 2(7), pages 301–319. DOI: 10.1002/2014EA000089.

Drob, D. P., M. Garcés, M. Hedlin, and N. Brachet (2010). "The Temporal Morphology of Infrasound Propagation". *Pure and Applied Geophysics* 167(4), pages 437–453. DOI: 10.1007/s00024-010-0080-6.

Drob, D. P., J. M. Picone, and M. Garcés (2003). "Global morphology of infrasound propagation". *Journal of Geophysical Research: Atmospheres* 108(D21). DOI: 10.1029/2002JD003307.

Dziak, R. P., D. R. Bohnenstiehl, and D. K. Smith (2012). "Hydroacoustic Monitoring of Oceanic Spreading Centers: Past, Present, and Future". *Oceanography* 25(1), pages 116–127.

Dziak, R. P., H. Matsumoto, S. Haver, D. K. Mellinger, L. Roche, J. H. Haxel, S. Stalin, C. Meinig, K. Kohlman, A. Sremba, J. Gedamke, L. Hatch, and S. Van Parijs (2023). "Pmel Passive Acoustics Research: Quantifying the Ocean Soundscape from Whales to Wave Energy". *Oceanography* 36(2/3), pages 196–205.

Ewing, M. and J. L. Worzel (1948). "LONG-RANGE SOUND TRANSMISSION". *Propagation of Sound in the Ocean*. Edited by J. L. Worzel, M. Ewing, and C. L. Pekeris. Volume 27. Geological Society of America, page 0. ISBN: 978-0-8137-1027-3. DOI: 10.1130/MEM27-3-p1.

Fauria, K. E., M. Jutzeler, T. Mittal, A. K. Gupta, L. J. Kelly, J. Rausch, R. Bennartz, B. Delbridge, and L. Retailleau (2023). "Simultaneous creation of a large vapor plume and pumice raft by the 2021 Fukutoku-Oka-no-Ba shallow submarine eruption". *Earth and Planetary Science Letters* 609, page 118076. DOI: 10.1016/j.epsl.2023.118076.

Fee, D. and R. S. Matoza (2013). "An overview of volcano infrasound: From hawaiian to plinian, local to global". *Journal of Volcanology and Geothermal Research* 249(C). ISBN: 03770273, pages 123–139. DOI: 10.1016/j.jvolgeores.2012.09.002.

Furukawa, H. (1992). "Annual report of the world volcanic eruptions in 1992". *Bulletin of Volcanic Eruptions* 57, pages 81–82.

Genareau, K., S. M. Cloer, K. Primm, M. A. Tolbert, and T. W. Woods (2018). "Compositional and Mineralogical Effects on Ice Nucleation Activity of Volcanic Ash". *Atmosphere* 9(7). Number: 7, page 238. DOI: 10.3390/atmos9070238.

Green, D. N., L. G. Evers, D. Fee, R. S. Matoza, M. Snellen, P. Smets, and D. Simons (2013). "Hydroacoustic, infrasonic and seismic monitoring of the submarine eruptive activity and sub-aerial plume generation at South Sarigan, May 2010". *Journal of Volcanology and Geothermal Research* 257. ISBN: 0377-0273, pages 31–43. DOI: 10.1016/j.jvolgeores.2013.03.006.

Gupta, A. K., R. Bennartz, K. E. Fauria, and T. Mittal (2022). "Eruption chronology of the December 2021 to January 2022 Hunga Tonga-Hunga Ha'apai eruption sequence". *Communications Earth & Environment* 3(1). Number: 1, pages 1–10. DOI: 10.1038/s43247-022-00606-3.

Gupta, A. K., T. Mittal, K. E. Fauria, R. Bennartz, and J. F. Kok (2025). "The January 2022 Hunga eruption cooled the southern hemisphere in 2022 and 2023". *Communications Earth & Environment* 6(1), pages 1–15. DOI: 10.1038/s43247-025-02181-9.

Hetzer, C., D. Drob, and K. Zabel (2024). *The NCPA-G2S request system*.

Hill, R. D. (1985). "Investigation of lightning strikes to water surfaces". *The Journal of the Acoustical Society of America* 78(6), pages 2096–2099. DOI: 10.1121/1.392668.

Hillger, D. W. and T. J. Schmit (2009). "THE GOES-13 SCIENCE TEST: A Synopsis". *Bulletin of the American Meteorological Society* 90(5), pages 592–597.

Ichihara, M., P. D. Mininni, S. Ravichandran, C. Cimarelli, and C. Vagasky (2023). "Multiphase turbulent flow explains lightning rings in volcanic plumes". *Communications Earth & Environment* 4(1). Number: 1, pages 1–12. DOI: 10.1038/s43247-023-01074-z.

Ito, K., S. Kato, M. Takahashi, and A. Saito (2011). "Volcanic topography of Fukutoku-Oka-no-Ba volcano in Izu-Ogasawara arc after the 2010 eruption". *Rep. Hydrogr. Oceanogr. Res.* 47, pages 9–13.

Jensen, F. B., W. A. Kuperman, M. B. Porter, and H. Schmidt (2011). *Computational Ocean Acoustics*. Modern Acoustics and Signal Processing. New York, NY: Springer New York. ISBN: 978-1-4419-8677-1 978-1-4419-8678-8. DOI: 10.1007/978-1-4419-8678-8.

Kahn, R. A., J. A. Limbacher, K. T. Junghenn Noyes, V. J. B. Flower, L. M. Zamora, and K. F. McKee (2024). "Evolving Particles in the 2022 Hunga Tonga—Hunga Ha'apai Volcano Eruption Plume". *Journal of Geophysical Research: Atmospheres* 129(11). DOI: 10.1029/2023JD039963.

Kuno, H. (1962). "Iwo-Zima (8,4 - 12)". *Catalogue of the active volcanoes of the world, including solfatara fields of Imperial Earthquake Investigation Committee*. Japan, Taiwan and Marianas XI. Rome, Italy: International Volcanological Association, pages 259–265.

Latter, J. H. (1979). "Volcanological observations at Tongariro National Park. II: Types and classification of volcanic earthquakes, 1976-1978". *Volcanological observations at Tongariro National Park. II: Types and classification of volcanic earthquakes, 1976-1978* (150). Place: Wellington, IV–60 p.

Lavayssière, A., S. Bazin, and J.-Y. Royer (2024). "Hydroacoustic Monitoring of Mayotte Submarine Volcano during Its Eruptive Phase". *Geosciences* 14(6). Number: 6, page 170. DOI: 10.3390/geosciences14060170.

Le Bras, R. J., M. Zampolli, D. Metz, G. Haralabus, P. Bittner, M. Villarroel, H. Matsumoto, G. Graham, and N. Meral Özel (2022). "The Hunga Tonga–Hunga Ha'apai Eruption of 15 January 2022: Observations on the International Monitoring System (IMS) Hydroacoustic Stations and Synergy with Seismic and Infrasound Sensors". *Seismological Research Letters* 94(2A), pages 578–588. DOI: 10.1785/0220220240.

Le Pichon, A., L. Ceranna, C. Pilger, P. Mialle, D. Brown, P. Herry, and N. Brachet (2013). "The 2013 Russian fireball largest ever detected by CTBTO infrasound sensors". *Geophysical Research Letters* 40(14), pages 3732–3737. DOI: 10.1002/grl.50619.

Lee, D.-C., J. V. Olson, and C. A. L. Szuberla (2013). "Computationally robust and noise resistant numerical detector for the detection of atmospheric infrasound". *The Journal of the Acoustical Society of America* 134(1), pages 862–868. DOI: 10.1121/1.4807802.

Li, J., P. R. White, B. Roche, J. M. Bull, T. G. Leighton, J. W. Davis, and J. W. Fone (2021). "Acoustic and optical determination of bubble size distributions – Quantification of seabed gas emissions". *International Journal of Greenhouse Gas Control* 108, page 103313. DOI: 10.1016/j.ijggc.2021.103313.

Liu, W. (, N. (Li, X.-l. (Huang, Y. (Kang, C. (Li, W. (Qiang, and C.-s. (Weng (2021). "Experimental study of underwater pulse detonation gas jets: Bubble velocity field and time–frequency characteristics of pressure field". *Physics of Fluids* 33(8), page 083324. DOI: 10.1063/5.0060686.

Lytaev, M. (2023). "Mesh Optimization for the Acoustic Parabolic Equation". *Journal of Marine Science and Engineering* 11(3). Number: 3, page 496. DOI: 10.3390/jmse11030496.

Maeno, F., T. Kaneko, M. Ichihara, Y. J. Suzuki, A. Yasuda, K. Nishida, and T. Ohminato (2022). "Seawater-magma interactions sustained the high column during the 2021 phreatomagmatic eruption of Fukutoku-Oka-no-Ba". *Communications Earth & Environment* 3(1), page 260. DOI: 10.1038/s43247-022-00594-4.

Mastin, L. G., A. R. Van Eaton, and S. J. Cronin (2024). "Did steam boost the height and growth rate of the giant Hunga eruption plume?" *Bulletin of Volcanology* 86(7), page 64. DOI: 10.1007/s00445-024-01749-1.

Maters, E. C., C. Cimarelli, A. S. Casas, D. B. Dingwell, and B. J. Murray (2020). "Volcanic ash ice-nucleating activity can be enhanced or depressed by ash-gas interaction in the eruption plume". *Earth and Planetary Science Letters* 551, page 116587. DOI: 10.1016/j.epsl.2020.116587.

Maters, E. C., D. B. Dingwell, C. Cimarelli, D. Müller, T. F. Whale, and B. J. Murray (2019). "The importance of crystalline phases in ice nucleation by volcanic ash". *Atmospheric Chemistry and Physics* 19(8), pages 5451–5465. DOI: 10.5194/acp-19-5451-2019.

Mather, T. A. and R. G. Harrison (2006). "Electrification of volcanic plumes". *Surveys in Geophysics* 27(4), pages 387–432. DOI: 10.1007/s10712-006-9007-2.

Mathews, L. T., K. L. Gee, and G. W. Hart (2021). "Characterization of Falcon 9 launch vehicle noise from far-field measurements". *The Journal of the Acoustical Society of America* 150(1), pages 620–633. DOI: 10.1121/10.0005658.

Matoza, R. S., D. Fee, M. A. Garcés, J. M. Seiner, P. A. Ramón, and M. A. H. Hedlin (2009). "Infrasonic jet noise from volcanic eruptions". *Geophysical Research Letters* 36(8). ISBN: 0094-8276, page L08303. DOI: 10.1029/2008GL036486.

Matoza, R. S., D. Fee, J. D. Assink, A. M. Iezzi, D. N. Green, K. Kim, L. Toney, T. Lecocq, S. Krishnamoorthy, J.-M. Lalande, K. Nishida, K. L. Gee, M. M. Haney, H. D. Ortiz, Q. Brissaud, L. Martire, L. Rolland, P. Vergados, A. Nippress, J. Park, S. Shani-Kadmiel, A. Witsil, S. Arrowsmith, C. Cau-

dron, S. Watada, A. B. Perttu, B. Taisne, P. Mialle, A. Le Pichon, J. Vergoz, P. Hupe, P. S. Blom, R. Waxler, S. De Angelis, J. B. Snively, A. T. Ringler, R. E. Anthony, A. D. Jolly, G. Kilgour, G. Averbuch, M. Ripepe, M. Ichihara, A. Arciniega-Ceballos, E. Astafyeva, L. Ceranna, S. Cevuard, I.-Y. Che, R. De Negri, C. W. Ebeling, L. G. Evers, L. E. Franco-Marin, T. B. Gabrielson, K. Hafner, R. G. Harrison, A. Komjathy, G. Lacanna, J. Lyons, K. A. Macpherson, E. Marchetti, K. F. McKee, R. J. Mellors, G. Mendo-Pérez, T. D. Mikesell, E. Munaibari, M. Oyola-Merced, I. Park, C. Pilger, C. Ramos, M. C. Ruiz, R. Sabatini, H. F. Schwaiger, D. Tailpied, C. Talmadge, J. Vidot, J. Webster, and D. C. Wilson (2022). "Atmospheric waves and global seismoacoustic observations of the January 2022 Hunga eruption, Tonga". *Science*. DOI: 10.1126/science.abo7063.

Matoza, R. S., D. Fee, T. B. Neilsen, K. L. Gee, and D. E. Ogden (2013). "Aeroacoustics of volcanic jets: Acoustic power estimation and jet velocity dependence". *Journal of Geophysical Research: Solid Earth* 118(12), pages 6269–6284. DOI: 10.1002/2013JB010303.

McKee, K., C. M. Smith, K. Reath, E. Snee, S. Maher, R. S. Matoza, S. Carn, L. Mastin, K. Anderson, D. Damby, D. C. Roman, A. Degterev, A. Rybin, M. Chibisova, J. D. Assink, R. de Negri Leiva, and A. Perttu (2021a). "Evaluating the state-of-the-art in remote volcanic eruption characterization Part I: Raikoke volcano, Kuril Islands". *Journal of Volcanology and Geothermal Research* 419, page 107354. DOI: 10.1016/j.jvolgeores.2021.107354.

McKee, K., C. M. Smith, K. Reath, E. Snee, S. Maher, R. S. Matoza, S. Carn, D. C. Roman, L. Mastin, K. Anderson, D. Damby, I. Itikarai, K. Mulina, S. Saunders, J. D. Assink, R. de Negri Leiva, and A. Perttu (2021b). "Evaluating the state-of-the-art in remote volcanic eruption characterization Part II: Ulawun volcano, Papua New Guinea". *Journal of Volcanology and Geothermal Research* 420, page 107381. DOI: 10.1016/j.jvolgeores.2021.107381.

McNutt, S. R. and D. C. Roman (2015). "Chapter 59 - Volcanic Seismicity". *The Encyclopedia of Volcanoes*. Edited by H. Sigurdsson. Elsevier Inc., pages 1011–1034.

Méndez Harper, J. and J. Dufek (2016). "The effects of dynamics on the triboelectrification of volcanic ash". *Journal of Geophysical Research: Atmospheres* 121(14), pages 8209–8228. DOI: 10.1002/2015JD024275.

Metz, D., A. B. Watts, I. Grevemeyer, M. Rodgers, and M. Paulatto (2016). "Ultra-long-range hydroacoustic observations of submarine volcanic activity at Monowai, Kermadec Arc". *Geophysical Research Letters* 43(4), pages 1529–1536. DOI: 10.1002/2015GL067259.

Metz, D. (2022). "Analysis of International Monitoring System hydrophone triplet data: Identifying the August 2021 eruption at Fukutoku-Okanoba, 24.3°N Bonin Arc". *Acoustical Science and Technology* 43(2), pages 125–128. DOI: 10.1250/ast.43.125.

Minakami, T. (1960). "Fundamental Research for Predicting Volcanic Eruptions (Part 1)". *Bulletin of the Earthquake Research Institute* 38, pages 497–544.

NAS (2017). *Volcanic Eruptions and Their Repose, Unrest, Precursors, and Timing*. Technical report. Publication Title: Volcanic Eruptions and Their Repose, Unrest, Precursors, and Timing. Washington, D.C.: National Academies Press, pages 1–122. DOI: 10.17226/24650.

National Centers for Environmental Prediction/National Weather Service/NOAA/U S. Department of Commerce (2015). *NCEP GFS 0.25 Degree Global Forecast Grids Historical Archive*. DOI: 10.5065/D65D8PWK.

Ohno, Y., A. Iguchi, M. Ijima, K. Yasumoto, and A. Suzuki (2022). "Coastal ecological impacts from pumice rafts". *Scientific Reports* 12(1), page 11187. DOI: 10.1038/s41598-022-14614-y.

Olson, J. V. and C. A. Szuberla (2008). "Processing Infrasonic Array Data". *Handbook of Signal Processing in Acoustics*. Edited by D. Havelock, S. Kuwano, and M. Vorlander. Volume 2. Section: 81. New York, NY: Springer, pages 1487–1496. ISBN: 978-0-387-77698-9.

Otani, Y., N. Sasahara, T. Yabuki, T. Hattori, S. Miyazaki, M. Oikawa, and K. Nogami (2006). "Observation on Fukutoku-Oka-no-Ba submarine volcano eruption in 2005". *Report of Hydrographic and Oceanographic Researches* 42, pages 31–37.

Perttu, A., C. Caudron, J. D. Assink, D. Metz, D. Tailpied, B. Perttu, C. Hibert, D. Nurfiani, C. Pilger, M. Muzli, D. Fee, O. L. Andersen, and B. Taisne (2020). "Reconstruction of the 2018 tsunamigenic flank collapse and eruptive activity at Anak Krakatau based on eyewitness reports, seismo-acoustic and satellite observations". *Earth and Planetary Science Letters* 541, page 116268. DOI: 10.1016/j.epsl.2020.116268.

Perttu, A., J. Assink, A. R. Van Eaton, C. Caudron, C. Vagasky, J. Krippner, K. McKee, S. De Angelis, B. Perttu, B. Taisne, and G. Lube (2023). "Remote Characterization of the 12 January 2020 Eruption of Taal Volcano, Philippines, Using Seismo-Acoustic, Volcanic Lightning, and Satellite Observations". *Bulletin of the Seismological Society of America*. DOI: 10.1785/0120220223.

Picone, J. M., A. E. Hedin, D. P. Drob, and A. C. Aikin (2002). "NRLMSISE-00 empirical model of the atmosphere: Statistical comparisons and scientific issues". *Journal of Geophysical Research: Space Physics* 107(A12), SIA 15–1–SIA 15–16. DOI: 10.1029/2002JA009430.

Pouget, S., M. Bursik, P. Webley, J. Dehn, and M. Pavolonis (2013). "Estimation of eruption source parameters from umbrella cloud or downwind plume growth rate". *Journal of Volcanology and Geothermal Research* 258, pages 100–112. DOI: 10.1016/j.jvolgeores.2013.04.002.

Prata, A. T., A. Folch, A. J. Prata, R. Biondi, H. Brenot, C. Cimarelli, S. Corradini, J. Lapierre, and A. Costa (2020). "Anak Krakatau triggers volcanic freezer in the upper troposphere". *Scientific Reports* 10(1). Bandiera_abtest: a Cc_license_type: cc_by Cg_type: Nature Research Journals Number: 1 Primary_atype: Research Subject_term: Natural hazards;Volcanology Subject_term_id: natural-hazards;volcanology, page 3584. DOI: 10.1038/s41598-020-60465-w.

Proud, S. R., A. T. Prata, and S. Schmauß (2022). "The January 2022 eruption of Hunga Tonga-Hunga Ha'apai volcano

reached the mesosphere". *Science* 378(6619), pages 554–557. DOI: 10.1126/science.abo4076.

Rienecker, M. M., M. J. Suarez, R. Todling, J. Bacmeister, L. Takacs, H.-C. Liu, W. Gu, M. Sienkiewicz, R. D. Koster, R. Gelaro, I. Stajner, and J. E. Nielsen (2008). *The GEOS-5 Data Assimilation System-Documentation of Versions 5.0.1, 5.1.0, and 5.2.0*. Technical report NASA/TM-2008-104606-VOL-27. NTRS Author Affiliations: Goddard Space Flight Center, Science Applications International Corporation, University of Maryland, Baltimore County, Science Systems and Applications, Inc., Science Applications International Corporation NTRS Document ID: 20120011955 NTRS Research Center: Goddard Space Flight Center (GSFC).

Roche, B., P. White, J. Bull, and T. G. Leighton (2022). "Measuring marine gas flux via passive acoustic signals—New field and lab observations". *The Journal of the Acoustical Society of America* 152(4_Supplement), A213. DOI: 10.1121/10.0016047.

Rowell, C. R., A. M. Jellinek, S. Hajimirza, and T. J. Aubry (2022). "External Surface Water Influence on Explosive Eruption Dynamics, With Implications for Stratospheric Sulfur Delivery and Volcano-Climate Feedback". *Frontiers in Earth Science* 10. DOI: 10.3389/feart.2022.788294.

Ryan, W. B. F., S. M. Carbotte, J. O. Coplan, S. O'Hara, A. Melkonian, R. Arko, R. A. Weissel, V. Ferrini, A. Goodwillie, F. Nitsche, J. Bonczkowski, and R. Zemsky (2009). "Global Multi-Resolution Topography synthesis". *Geochemistry, Geophysics, Geosystems* 10(3). _eprint: https://onlinelibrary.wiley.com/doi/pdf/10.1029/2008GC002332. DOI: 10.1029/2008GC002332.

Said, R. K., M. B. Cohen, and U. S. Inan (2013). "Highly intense lightning over the oceans: Estimated peak currents from global GLD360 observations". *Journal of Geophysical Research: Atmospheres* 118(13), pages 6905–6915. DOI: 10.1002/jgrd.50508.

Schmit, T. J., P. Griffith, M. M. Gunshor, J. M. Daniels, S. J. Goodman, and W. J. Lebair (2017). "A Closer Look at the ABI on the GOES-R Series". *Bulletin of the American Meteorological Society* 98(4), pages 681–698. DOI: 10.1175/BAMS-D-15-00230.1.

Schmit, T. J., M. M. Gunshor, W. P. Menzel, J. J. Gurka, J. Li, and A. S. Bachmeier (2005). "INTRODUCING THE NEXT-GENERATION ADVANCED BASELINE IMAGER ON GOES-R". *Bulletin of the American Meteorological Society* 86(8), pages 1079–1096. DOI: 10.1175/BAMS-86-8-1079.

Schneider, D. J., A. R. Van Eaton, and K. L. Wallace (2020). "Satellite observations of the 2016–2017 eruption of Bogoslof volcano: aviation and ash fallout hazard implications from a water-rich eruption". *Bulletin of Volcanology* 82(3), page 29. DOI: 10.1007/s00445-020-1361-2.

Smith, C. M., A. R. V. Eaton, D. J. Schneider, L. Mastin, R. S. Matoza, K. McKee, and S. Maher (2022). "Spatial analysis of globally detected volcanic lightning from the June 2019 eruption of Raikoke volcano, Kuril Islands". *Volcanica* 5(2), pages 385–395. DOI: 10.30909/vol.05.02.385395.

Smith, C. M., D. Gaudin, A. R. Van Eaton, S. A. Behnke, S. Reader, R. J. Thomas, H. Edens, S. R. McNutt, and C. Cimarelli (2021). "Impulsive Volcanic Plumes Generate Volcanic Lightning and Vent Discharges: A Statistical Analysis of Sakurajima Volcano in 2015". *Geophysical Research Letters* 48(11), e2020GL092323. DOI: 10.1029/2020GL092323.

Stix, J. (2018). "Understanding Fast and Slow Unrest at Volcanoes and Implications for Eruption Forecasting". *Frontiers in Earth Science* 6. DOI: 10.3389/feart.2018.00056.

Sutherland, L. C. and H. E. Bass (2004). "Atmospheric absorption in the atmosphere up to 160 km". *The Journal of the Acoustical Society of America* 115(3), pages 1012–1032. DOI: 10.1121/1.1631937.

Suzuki, Y. J. and T. Koyaguchi (2009). "A three-dimensional numerical simulation of spreading umbrella clouds". *Journal of Geophysical Research: Solid Earth* 114(B3), 2007JB005369. DOI: 10.1029/2007JB005369.

Tam, C. K. W., K. Viswanathan, K. K. Ahuja, and J. Panda (2008). "The sources of jet noise: experimental evidence". *Journal of Fluid Mechanics* 615. ISBN: 0022-1120, pages 253–292. DOI: 10.1017/S0022112008003704.

Tanaka, S., M. Nakano, T. Nakajima, J. Yoshimitsu, M. Obayashi, and D. Metz (2025). "Monitoring Submarine Volcanic Activities in the Izu–Bonin–Mariana Arc Using the International Monitoring System Hydrophone Array Signals". *Seismological Research Letters*. DOI: 10.1785/0220240341.

Tani, K., O. Ishizuka, H. Minami, T. Oikawa, H. Katayama, Y. Suzuki, T. Shimano, M. Nagai, I. McIntosh, F. Maeno, M. Nakamura, N. Jimi, T. Mizuno, T. Ukita, F. Ikegami, and T. Sano (2022). *August 2021 eruption of the Fukutoku Oka-na-Ba volcano, Izu-Bonin Arc: Latest results from the rapid response seafloor surveys*.

Tepp, G. and R. P. Dziak (2021). "The Seismo-Acoustics of Submarine Volcanic Eruptions". *Journal of Geophysical Research: Solid Earth* 126(4), e2020JB020912. DOI: 10.1029/2020JB020912.

Tepp, G., R. P. Dziak, M. M. Haney, J. J. Lyons, C. Searcy, H. Matsumoto, and J. Haxel (2020). "Seismic and hydroacoustic observations of the 2016–17 Bogoslof eruption". *Bulletin of Volcanology* 82(1). DOI: 10.1007/s00445-019-1344-3.

Urai, M. (2014). "Time series analysis of discolored seawater reflectance observed by Advanced Visible and Near Infrared Radiometer type 2 (AVNIR-2) at Fukutoku-Okanoba submarine volcano, Japan". *Journal of Volcanology and Geothermal Research* 269, pages 23–27. DOI: 10.1016/j.jvolgeores.2013.11.006.

Van Eaton, A. R., M. Herzog, C. J. Wilson, and J. McGregor (2012). "Ascent dynamics of large phreatomagmatic eruption clouds: The role of microphysics". *Journal of Geophysical Research: Solid Earth* 117(3), pages 1–23. DOI: 10.1029/2011JB008892.

Van Eaton, A. R., Á. Amigo, D. Bertin, L. G. Mastin, R. E. Giacosa, J. González, O. Valderrama, K. Fontijn, and S. A. Behnke (2016). "Volcanic lightning and plume behavior reveal evolving hazards during the April 2015 eruption of Calbuco volcano, Chile". *Geophysical Research Letters* 43(7), pages 3563–3571. DOI: 10.1002/2016GL068076.

Van Eaton, A. R., J. Lapierre, S. A. Behnke, C. Vagasky, C. J. Schultz, M. Pavolonis, K. Bedka, and K. Khlopenkov (2023). "Lightning Rings and Gravity Waves: Insights Into the Giant Eruption Plume From Tonga's Hunga Volcano on 15 January 2022". *Geophysical Research Letters* 50(12), e2022GL102341. DOI: 10.1029/2022GL102341.

Van Eaton, A. R., D. J. Schneider, C. M. Smith, M. M. Haney, J. J. Lyons, R. Said, D. Fee, R. H. Holzworth, and L. G. Mastin (2020). "Did ice-charging generate volcanic lightning during the 2016–2017 eruption of Bogoslof volcano, Alaska?" *Bulletin of Volcanology* 82(3). DOI: 10.1007/s00445-019-1350-5.

Van Eaton, A. R., C. M. Smith, M. Pavolonis, and R. Said (2022). "Eruption dynamics leading to a volcanic thunderstorm—The January 2020 eruption of Taal volcano, Philippines". *Geology* 50(4), pages 491–495. DOI: 10.1130/G49490.1.

Vömel, H., S. Evan, and M. Tully (2022). "Water vapor injection into the stratosphere by Hunga Tonga-Hunga Ha'apai". *Science* 377(6613), pages 1444–1447. DOI: 10.1126/science.abq2299.

Wakimizu, T. (1908). "The ephemeral volcanic island in the Iwojima Group". *Earthquake Investigation Committee* 22, pages 1–33.

Waxler, R. and J. Assink (2019). "Propagation Modeling Through Realistic Atmosphere and Benchmarking". *Infrasound Monitoring for Atmospheric Studies: Challenges in Middle Atmosphere Dynamics and Societal Benefits*. Edited by A. Le Pichon, E. Blanc, and A. Hauchecorne. Cham: Springer International Publishing, pages 509–549. ISBN: 978-3-319-75140-5. DOI: 10.1007/978-3-319-75140-5_15.

Waxler, R., J. Assink, and D. Velea (2017). "Modal expansions for infrasound propagation and their implications for ground-to-ground propagation". *The Journal of the Acoustical Society of America* 141(2), pages 1290–1307. DOI: 10.1121/1.4976067.

Wech, A., G. Tepp, J. Lyons, and M. M. Haney (2018). "Using Earthquakes, T Waves, and Infrasound to Investigate the Eruption of Bogoslof Volcano, Alaska". *Geophysical Research Letters* 45(14), pages 6918–6925. DOI: 10.1029/2018GL078457.

Yoshida, K., Y. Tamura, T. Sato, T. Hanyu, Y. Usui, Q. Chang, and S. Ono (2022). "Variety of the drift pumice clasts from the 2021 Fukutoku-Oka-no-Ba eruption, Japan". *Island Arc* 31(1), e12441. DOI: 10.1111/iar.12441.